Hepatocellular Carcinoma in Patients with Chronic Liver Disease: Comparison of SPIO-enhanced MR Imaging and 16–Detector Row CT[1]

Young Kon Kim, MD
Hyo Sung Kwak, MD
Chong Soo Kim, MD
Gyung Ho Chung, MD
Young Min Han, MD
Jeong Min Lee, MD

Purpose: To compare the sensitivity, positive predictive value, and diagnostic accuracy of superparamagnetic iron oxide (SPIO)-enhanced magnetic resonance (MR) imaging with those of 16–detector row computed tomography (CT) for the detection of hepatocellular carcinoma (HCC) in patients with hepatitis B–induced cirrhosis.

Materials and Methods: Institutional Review Board approval was obtained for this study, and informed consent was obtained from all patients. A total of 44 patients (36 men, eight women; age range, 35–67 years) with 59 HCCs and mild liver cirrhosis (Child-Pugh score A or B) underwent multiphasic CT and SPIO-enhanced MR imaging. The diagnosis of HCC was established at surgical resection ($n = 31$) and percutaneous biopsy ($n = 28$). SPIO-enhanced MR imaging was composed of T2-weighted turbo spin-echo and T2*-weighted gradient-echo sequences. Multiphasic CT consisted of four phases (ie, early arterial, late arterial, portal venous, and equilibrium). Three observers independently analyzed each image in random order. Sensitivity, positive predictive value, and diagnostic accuracy were calculated by using the alternative free-response receiver operating characteristic analysis for multi–detector row CT and SPIO-enhanced MR imaging.

Results: Although not significant ($P > .05$), the area under the receiver operating characteristic curve for SPIO-enhanced MR imaging (mean, 0.90) was higher than that for multi–detector row CT (mean, 0.82) for all observers. Also, although no significant difference was demonstrated by any of the three observers ($P > .05$), there was a trend toward increased sensitivity on both a per-lesion and a per-patient basis for SPIO-enhanced MR imaging (mean, 84.7% and 94.7%, respectively) compared with multi–detector row CT (mean, 76.9% and 88.6%, respectively). No significant difference in positive predictive value was observed between modalities.

Conclusion: SPIO-enhanced MR imaging and multiphasic CT show similar diagnostic accuracy, sensitivity, and positive predictive value for the detection of HCC in patients with relatively mild hepatitis B–induced cirrhosis.

[1] From the Department of Diagnostic Radiology, Chonbuk National University Medical School and Hospital, Jeonju, Korea (Y.K.K., H.S.K., C.S.K., G.H.C., Y.M.H.); and Department of Radiology, Seoul National University College of Medicine, 28, Yongon-Dong, Chongno-Gu, Seoul 110-744, Korea (J.M.L.). Received December 27, 2004; revision requested February 24, 2005; revision received April 21; accepted May 27; final version accepted July 1.

Advances in various imaging modalities, including ultrasonography (US), computed tomography (CT), and magnetic reosnance (MR) imaging, have facilitated the detection of hepatocellular carcinoma (HCC) at a preclinical stage (1–3). As a result, the resectability of HCC has markedly increased during the past two decades, thereby significantly improving survival (4,5). Liver resection remains a good treatment for HCC in patients with cirrhosis, but local methods of tumor ablation, including transarterial chemoembolization, percutaneous ethanol injection, and radiofrequency ablation, are promising extensions of tumor therapy for patients with limited liver function or unresectable multifocal tumors (6–9). Regardless of the therapeutic modalities used, it is well known that the best results are obtained in patients with small, noninvasive tumors (10). Therefore, it is important to choose an imaging modality that has the highest sensitivity for the detection of HCC.

During the past decade, multiphasic dynamic CT and MR imaging have had central roles in the evaluation of focal liver lesions. With the development of a variety of tissue-specific MR contrast agents, such as superparamagnetic iron oxide (SPIO) or gadobenate dimeglumine, contrast material–enhanced MR imaging of the liver has begun to be regarded as a more accurate noninvasive imaging modality than biphasic helical CT (11–16). The previous introduction of the multi–detector row CT scanner for liver imaging, however, has allowed the acquisition of optimum dynamic images with high temporal and high z-axis resolution; this raises the expectation of further improvements in the diagnostic accuracy of liver CT imaging comparable to or better than that of liver MR imaging for the evaluation of HCC (17–19).

Data from several reports have demonstrated that the diagnostic accuracy or sensitivity of SPIO-enhanced MR imaging is higher than that of dynamic CT for the detection of HCC (20–23). To our knowledge, however, there has been no comparative study between SPIO-enhanced MR imaging and 16–detector row CT for the detection of HCC with acquisition of double arterial phase images. The purpose of our study, therefore, was to compare the sensitivity, positive predictive value, and diagnostic accuracy of SPIO-enhanced MR imaging with those of 16–detector row CT for the detection of HCC in patients with hepatitis B–induced cirrhosis.

Materials and Methods

Patient Population

Between September 2003 and June 2004, 67 patients (43 men, 24 women; age range, 35–76 years; mean age, 57 years) who were suspected of having HCC after review of clinical and prior US findings underwent multiphasic contrast-enhanced dynamic multi–detector row CT and SPIO-enhanced MR imaging at Chonbuk National University Hospital, which is a tertiary referral hospital. Underlying liver cirrhosis was related to viral hepatitis B in 64 patients, viral hepatitis C in two patients, and alcoholic cirrhosis in one patient. The severity of liver cirrhosis was based on the Child-Pugh classification (24), with 49 patients classified as Child-Pugh class A, 16 as Child-Pugh class B, and the remaining two as Child-Pugh class C. Written informed consent was obtained from each patient before they entered into the study, and the institutional review board of our hospital approved the study.

For the 67 study patients, final inclusion criteria were *(a)* multiphasic contrast-enhanced dynamic multi–detector row CT and SPIO-enhanced MR imaging performed within a 10-day interval (mean, 4 days), *(b)* presence of histologically proved nodular HCC at surgery or image-guided percutaneous biopsy, and *(c)* follow-up contrast-enhanced CT or MR imaging performed at least 5 months after the initial imaging examination. A total of 23 of the 67 patients were excluded from our study; 17 had no histologic proof of HCC, two had massive or infiltrative HCCs that involved more than two segments of the liver, two had too many (ie, more than 10) nodules to be analyzed, and two had not undergone follow-up contrast-enhanced CT or MR imaging. Therefore, the remaining 44 patients (36 men, eight women; age range, 35–67 years; mean age, 56 years) with HCCs formed the final study group. All patients had liver cirrhosis associated with viral hepatitis B. No patients with viral hepatitis C, viral hepatitis A, or alcoholic cirrhosis were included in this study. No study patients had liver masses other than the HCCs, regenerating nodules, and hepatic cysts. In all of these patients, liver cirrhosis was determined by means of clinical findings; blood tests that measured aspartate aminotransferase, alanine aminotransferase, alkaline phosphatase, bilirubin, albumin, and globulin levels; and histologic examination (35 patients). A total of 35 patients were classified as having Child-Pugh class A cirrhosis, and the remaining nine patients were classified as having Child-Pugh class B cirrhosis.

Lesion Confirmation: Reference Standard

A total of 44 patients with 59 pathologically proved tumors (diameter range, 0.6–6.6 cm; mean, 1.8 cm) were included in this study. Twenty-nine patients had one lesion each, and 15 patients had two lesions each. The final

Published online before print
10.1148/radiol.2381042193

Radiology 2006; 238:531–541

Abbreviations:
A_z = area under the ROC curve
FISP = fast imaging with steady-state precession
HCC = hepatocellular carcinoma
ROC = receiver operating characteristic
SPIO = superparamagnetic iron oxide

Author contributions:
Guarantors of integrity of entire study, Y.K.K., C.S.K., J.M.L.; study concepts/study design or data acquisition or data analysis/interpretation, all authors; manuscript drafting or manuscript revision for important intellectual content, all authors; approval of final version of submitted manuscript, all authors; literature research, Y.K.K.; clinical studies, all authors; statistical analysis, Y.K.K., H.S.K.; and manuscript editing, Y.K.K., J.M.L.

Address correspondence to J.M.L.
(e-mail: *leejm@radcom.snu.ac.kr*).

Authors stated no financial relationship to disclose.

diagnosis of HCC was proved by obtaining surgical specimens in 25 patients and by performing core needle biopsy in 19 patients.

Determination of the total number of lesions in the 25 patients with 31 HCCs who underwent hepatic resection was based on pathologic analysis of the surgical specimens and on the results of intraoperative US. All hepatic surgeries were performed by one experienced hepatobiliary surgeon with 20 years of experience in liver surgery. At the time of surgery, the surgeon (12 years of experience with intraoperative US) performed intraoperative US of the entire liver by using dedicated intraoperative US in all study patients. The average time interval between surgery and the last imaging examination was 9 days (range, 4–15 days). Before surgery, the location and number of liver masses at preoperative CT or MR imaging were carefully and jointly reviewed by the surgeon and by one radiologist (Y.M.H., with 15 years of experience in both hepatobiliary intervention and liver imaging).

After resection of the liver mass (segmentectomy, 15 patients; enucleation, 13 patients), the histopathologic results of the resected hepatic specimens were correlated with the preoperative imaging findings obtained by the radiologist. If additional hepatic nodules were found at intraoperative US or palpation, the hepatobiliary pathologist immediately performed frozen section analysis. For frozen section analysis, a surgical specimen that was quickly frozen at a −20°C was stained with hematoxylin-eosin; in this way, three additional HCCs that were not detected at either CT or MR imaging were found in three patients. One of the lesions was a daughter nodule that measured 0.6 cm in diameter and was located adjacent to the main HCC, which measured 3 cm in diameter; this daughter nodule was proved to be a moderately differentiated HCC. The other two lesions, which measured 2 and 0.9 cm in diameter, were hypovascular HCCs that were detected at CT during arterial portography; these two lesions proved to be well-differentiated HCCs. For the 25 patients who underwent hepatic surgery, follow-up images were used to ascertain the absence of a tumor nodule in the remaining liver after resection with intraoperative US.

The total number of tumor nodules in the 13 patients with 22 lesions who underwent transarterial chemoembolization was determined on the basis of a combination of results from image-guided biopsy (n = 22), CT hepatic arteriography and CT during arterial portography (n = 7), and CT performed after the administration of iodized oil (Lipiodol; Guerbet, Aulnay-sous-Bois, France) (n = 22), which was performed after transarterial chemoembolization and during follow-up CT or MR imaging at least 5 months after the initial imaging examination (n = 22). For CT performed after the administration of iodized oil (25), hepatic angiography was performed by one interventional radiologist (Y.M.H.) by using a digital angiographic unit (Angiostar; Siemens, Erlangen, Germany). Next, an emulsion of 5–10 mL of iodized oil with anticancer drugs was injected through a catheter while the tip of the catheter was placed superselectively into the segmental or subsegmental arteries that fed the tumor. On a CT scan of the liver that was obtained 1 month after the procedure, the nodular areas of retained iodized oil were diagnosed as HCC by the consensus of three radiologists (C.S.K., Y.K.K., H.S.K.). At follow-up contrast-enhanced CT or MR imaging, there were no newly growing tumors except for the 22 tumors that were found in the 13 study patients.

Diagnosis of HCC in the remaining six patients with six lesions who underwent radiofrequency thermal ablation was based on the results of imaged-guided biopsy and on the findings of follow-up CT or MR imaging performed at least 5 months after the initial imaging examination. In one patient, diagnosis of HCC was based on the results of hepatic angiography. On follow-up images, no newly growing liver masses were found, and so the total number of lesions in each patient was regarded as one. Follow-up contrast-enhanced CT or MR imaging was performed for a minimum of 6 months (range, 6–10 months) in all patients.

MR Imaging

All MR imaging examinations were performed by using a 1.5-T superconducting imager (Magnetom Symphony; Siemens) with a phased-array multicoil for signal reception. The liver was imaged in the transverse plane for all imaging sequences. Baseline MR imaging included a respiratory-triggered T2-weighted turbo spin-echo sequence, a breath-hold T2*-weighted fast imaging with steady-state precession (FISP) sequence, and a breath-hold T1-weighted fast low-angle shot sequence. Respiratory-triggered T2-weighted turbo spin-echo imaging was performed by using 3300–5500/85 (repetition time msec/echo time msec), an echo train length of five, a matrix of 256 × 512, and two signals acquired. Breath-hold T2*-weighted FISP was performed by using 180/12, a flip angle of 30°, a matrix of 96 × 256, and one signal acquired. Breath-hold T1-weighted fast low-angle shot imaging was performed by using 120/4, a flip angle of 70°, a matrix of 120 × 256, and one signal acquired. For all sequences, a 6-mm section thickness was used with a 10% intersection gap and a field of view of 35–40 cm, depending on the size of the liver.

SPIO-enhanced MR imaging comprised a respiratory-triggered T2-weighted turbo spin-echo sequence and a breath-hold T2*-weighted FISP sequence, both of which were performed by using the same parameters as those used in baseline MR imaging. The SPIO agent (Resovist; Schering, Berlin, Germany), which was administered at a dose of 8 μmol of iron per kilogram of body weight, was rapidly injected intravenously through a 5-μm filter (1 mL/sec) and was followed by a 15-mL flush of sterile saline solution. Imaging commenced approximately 10 minutes after intravenous injection of the SPIO agent.

Multi–Detector Row CT

CT examinations were performed by using a 16–detector row CT scanner (Sensation 16; Siemens). Images were acquired through the liver in a craniocaudal direction with a 1.5 × 16 beam collimation. Other scanning parameters were as follows: 160 mAs; 120 kVp;

detector collimation, 1.5 mm; table speed, 24 mm per rotation; and gantry rotation time, 0.5 second. A reconstruction section thickness of 3.0 mm and a reconstruction interval of 3.0 mm were used. Before the examinations, patients were instructed to hold their breath to avoid motion artifacts.

Unenhanced multi–detector row CT was performed first and began at the top of the liver in a craniocaudal direction. After acquisition of unenhanced liver images, contrast medium with a concentration of 370 mg of iodine per milliliter (iopromide, Ultravist 370; Schering) was administered, and a 40-mL flush of sterile saline was performed by using a power injector (Multilevel CT; Medrad, Pittsburgh, Pa). The contrast medium and saline solution were injected at a rate of 3 mL/sec through an 18-gauge plastic intravenous catheter that was placed in an antecubital vein. The volume of contrast medium (2 mL per kilogram of body weight) varied depending on the body weight of each patient; therefore, the total volume of contrast medium administered was 110–150 mL (mean, 120 mL ± 10 [standard deviation]). Determination of the scanning delay for arterial phase imaging was achieved by using an automatic bolus tracking technique (Siemens). Single-level monitoring low-dose scanning (120 kVp, 20 mA) was initiated 10 seconds after contrast material injection. Contrast material enhancement was automatically calculated in by placing the region of interest cursor over the vessel of interest (abdominal aorta), and the level of trigger threshold was set at an increase of 80 HU. Five seconds after the trigger threshold had been reached, the early arterial phase scanning began automatically. The dynamic images consisted of four phases (ie, early arterial, late arterial, portal venous, and equilibrium). The early and late arterial phases were acquired separately during each breath hold by using a minimum interscan delay (5 seconds). The start time of the late arterial phase was fixed at 12 seconds after the start time of the early arterial phase. The mean scanning time delays of the early and late arterial phases were 23 seconds and 35 seconds, respectively. The portal venous and equilibrium phases were acquired at 70 seconds and 180 seconds, respectively, after administration of contrast medium. The acquisition time for each phase was 7–10 seconds according to patient body size.

Imaging Analysis

Three faculty-level gastrointestinal radiologists (C.S.K., Y.K.K., and H.S.K., with 20, 8, and 8 years of experience, respectively) independently read the CT and MR images. During the review process, the observers were blinded to patient identifiers. All images were reviewed on a 2000 × 2000 picture archiving and communication systems monitor (PACS; Marotech, Seoul, Korea). The readers were free to alter the window level and window width at their discretion. They were aware of the overall goal of the study before the reading session and knew that the patients had liver cirrhosis and were at risk for HCC. Observers were unaware, however, of the presence or location of any liver lesions or of the results of other imaging examinations. Two separate sessions of image analysis were performed. In the first session, either the SPIO-enhanced MR image set (unenhanced T1-weighted and T2-weighted images and contrast-enhanced T2-weighted and T2*-weighted images) or the multi–detector row CT image set (unenhanced CT images and early arterial, late arterial, portal venous, and equilibrium phases) was randomly presented (ie, without any specific patient order). Only one image set (ie, either the CT or MR images of the same patients) was presented at a reading session. In the second session, the remaining CT and MR image sets were randomly presented as in the first session. To minimize any learning bias, we employed an interval of at least 4 weeks between the two readings sessions.

The criteria for hypervascular HCC at multi–detector row CT were defined as nodules that *(a)* showed contrast-enhanced foci during the early and/or late arterial phases and *(b)* demonstrated washout during portal venous and equilibrium phases. In addition, the diagnostic criteria for hypovascular HCC at multi–detector row CT were defined as nodules that *(a)* measured larger than 1 cm, *(b)* showed hypoattenuation during all dynamic phases with and/or without capsular enhancement during the equilibrium phase, and *(c)* did not fulfill the diagnostic criteria for a cyst (ie, smooth margins, homogeneous low attenuation similar to that of water, and no enhancement during the contrast-enhanced examination).

The criterion for HCC at SPIO-enhanced MR imaging was defined as a focal discrete nodular area that demonstrated high signal intensity relative to that of the adjacent liver parenchyma (ie, lower than the signal intensity of cerebrospinal fluid or the gallbladder on T2-weighted turbo spin-echo images to exclude a cyst) on both T2-weighted SPIO-enhanced MR images.

Each observer recorded the presence and segment location of the HCC lesions by using a four-point scale to assign a confidence level to each lesion. A confidence level of 1 was defined as "probably not an HCC lesion," a confidence level of 2 was defined as "a possible HCC lesion," a confidence level of 3 was defined as "a probable HCC lesion," and a confidence level of 4 was defined as "a definite HCC lesion." To achieve an accurate correlation between the findings of the scored lesions and the reference standard, including intraoperative US, iodized oil CT, CT hepatic angiography, CT during arterial portography, and follow-up imaging, each observer recorded the individual image number, the locations of all lesions, and the diameter of each lesion. For patients with multiple lesions located in the same segment, the observers added further description regarding the size and location of the lesion within each segment in order to avoid confusion in the data analysis. After the three observers completed the review sessions, the study coordinator (J.M.L, with 12 years of experience in abdominal imaging) together with two observers (Y.K.K, H.S.K) compared the scoring results of each observer with the reference standard and devised a possible explanation for the causes of the false-

positive and false-negative findings by each observer.

Statistical Analysis

Based on the reviews of the three observers, a alternative free-response receiver operating characteristic (ROC) curve analysis was performed on a tumor-by-tumor basis (26). For each image set, an alternative free-response ROC curve was fitted to each observer's confidence rating by using a maximum likelihood estimation program (ROCKIT 0.9B; *http://www-radiology.uchicago.edu/krl/KRL_ROC/*) (27). The diagnostic accuracy of each image set for each observer and the composite data were calculated by measuring the area under the alternative free-response ROC curve (A_z). The differences between image sets in terms of the mean A_z value were statistically analyzed by using the two-tailed Student t test for paired data. The sensitivity for detection of HCC on a per-lesion and per-patient basis and the positive predictive value for each image set were then calculated. To provide a range of plausible differences in sensitivity, 95% confidence intervals were also calculated (28). True-positive lesions were considered to be those that were assigned a confidence level of 3 or 4 by the observers but were confirmed to be HCC. False-negative lesions were considered to be those that were assigned a confidence level of 1 or 2 but were actually proved to be a lesion. The sensitivity and positive predictive value of both CT and MR images were compared by using the McNemar test. A two-tailed P value of less than .05 was considered to indicate a statistically significant difference.

To assess interobserver agreement for the evaluation of the two imaging modalities, we calculated the κ statistic for multiple observers (29). Agreement between blinded observers is reported below in terms of κ values, with κ values greater than 0 indicating a positive correlation. A κ value of less than 0.200 indicated positive but poor agreement; 0.210–0.400, fair agreement; 0.410–0.600, moderate agreement; 0.610–0.800, good agreement; and greater than 0.810, excellent agreement. The level for statistical significance was $P < .05$. The statistical analyses were calculated by using a commercially available software program (SPSS 8.0; SPSS, Chicago, Ill).

Results

ROC Analysis

For all observers, the A_z values (Table 1) for SPIO-enhanced MR imaging were slightly higher than those for multi–detector row CT. No statistically significant difference in the A_z value between both image sets was demonstrated by any of the three observers (mean A_z value for SPIO-enhanced MR imaging, 0.90; mean A_z value for multi–detector row CT, 0.82) ($P > .05$).

Sensitivity and Positive Predictive Value

Overall, there was a trend toward increased sensitivity (Table 2) on both a per-lesion and a per-patient basis for SPIO-enhanced MR imaging (mean, 84.7% and 94.7%, respectively) compared with multi–detector row CT (mean, 76.9% and 88.6%, respectively); a statistically significant difference between these two values, however, was not demonstrated by any of the three observers on a per-lesion (observers 1 and 2, $P = .06$; observer 3, $P = .13$) or per-patient (observers 1 and 2, $P = .25$; observer 3, $P = .50$) basis (Fig 1). Among the 59 total HCCs, 50 lesions (sensitivity, 84.7%; 95% confidence interval: 73.0%, 92.8%) were identified at SPIO-enhanced MR imaging by all observers. Multi–detector row CT facilitated the identification of 45 lesions by observers 1 and 2 (sensitivity, 76.3%; 95% confidence interval: 63.4%, 86.4%) and of 46 lesions by observer 3 (sensitivity, 78.0%; 95% confidence interval: 65.3%, 87.7%). In a per-patient analysis, SPIO-enhanced MR imaging depicted HCC in 42 patients for observers 1 and 2 (sensitivity, 95.5%; 95% confidence interval: 84.5%, 99.3%) and in 41 patients for observer 3 (sensitivity, 93.2%; 95% confidence interval: 81.3%, 98.5%). Multi–detector row CT depicted HCC in 39 patients for all three observers (sensitivity, 88.6%; 95% confidence interval: 75.4%, 96.2%).

False-Negative Findings: Multi–Detector Row CT and MR Imaging

There were nine lesions in seven patients that were not detected by any observers at multi–detector row CT but were revealed at SPIO-enhanced MR imaging (Figs 1, 2). Five of these nine lesions were confirmed at surgery, and the others were confirmed at image-guided biopsy. On retrospective review of multi–detector row CT images, all nine lesions were less than 10 mm in diameter (0.6–0.9 cm) and were considered to be hypovascular HCCs at MR imaging because they showed subtle low attenuation in at least one of the four dynamic phases (Figs 1, 2). Conversely, four lesions (0.8–1.5 cm in diameter) in four patients were not detected by any observers at SPIO-enhanced MR imaging but were detected by observers at multi–detector row CT (Fig 3). One of these lesions was confirmed at surgery and was proved to be a well-differentiated HCC. The other lesions were confirmed at image-guided biopsy with nodular iodized oil uptake after transarterial chemoembolization. These lesions were hypervascular HCCs that showed

Table 1

A_z Values Obtained with SPIO-enhanced MR Imaging and Multi–Detector Row CT for the Detection of HCC

Observer	SPIO-enhanced MR Imaging	Multi–Detector Row CT	Difference in A_z Values	P Value
1	0.89 ± 0.05	0.82 ± 0.07	0.08 ± 0.07	.30
2	0.90 ± 0.05	0.82 ± 0.07	0.08 ± 0.07	.25
3	0.91 ± 0.05	0.82 ± 0.07	0.09 ± 0.07	.25

Note.—All A_z values are presented as the mean ± standard deviation.

nodular enhancement and nodular staining during the arterial phases of multi–detector row CT and hepatic angiography. When we retrospectively reviewed the four missed lesions at SPIO-enhanced MR imaging, all lesions were masked by surrounding fibrosis or showed faint and irregular areas of high signal intensity with poor conspicuity (Fig 3).

There were four small HCCs that were not detected by any observers at either SPIO-enhanced MR imaging or multi–detector row CT. Three of these HCCs were found at intraoperative US and were then proved at surgery and pathologic examination. The other lesion was found at CT hepatic angiography and was confirmed with image-guided biopsy. When we retrospectively reviewed all of the images, three lesions were not depicted at either CT or MR imaging, and one lesion was missed owing to its location in the liver margin.

For positive predictive values, there was no significant difference between SPIO-enhanced MR imaging and multi–detector row CT ($P > .05$). For all observers, four false-positive findings at SPIO-enhanced MR imaging and seven false-positive findings at multi–detector row CT were found. False-positive findings at SPIO-enhanced MR imaging and multi–detector row CT were attributed to the fibrosis and arterioportal shunt, respectively.

For SPIO-enhanced MR imaging and multi–detector row CT, the κ values for the three observers were 0.740–0.893, indicating good or excellent interobserver agreement with regard to the presence of lesions (Table 3).

Discussion

We hypothesized that the diagnostic accuracy of 16–detector row CT with a highly concentrated iodine contrast agent (30) could be comparable to that of SPIO-enhanced MR imaging for the evaluation of HCC. To our knowledge, ours is the first comparative study of SPIO-enhanced MR imaging and 16–detector row CT that uses a multiphasic technique for the detection of HCC. We used two types of T2-weighted imaging sequences for SPIO-enhanced MR imaging—that is, a T2-weighted turbo spin-echo sequence with a 512 matrix for high-resolution imaging and a T2*-weighted gradient-recalled echo sequence for maximum lesion-to-liver contrast. The T2*-weighted gradient-recalled echo sequence has been accepted as the optimal pulse sequence because of its greater susceptibility resulting from local field inhomogeneity (31,32). For multi–detector row CT, double arterial phases were acquired in 3-mm reconstruction intervals by using a 1.5-mm detector collimation and a highly concentrated iodine contrast agent.

In the alternative free-response ROC analysis of our study, all three observers achieved higher diagnostic performance with SPIO-enhanced MR imaging than with multi–detector row CT, but the difference between the two techniques was not statistically significant for all observers ($P > .05$). Overall, a trend was seen toward a more greatly increased sensitivity with SPIO-enhanced MR imaging than with multi–detector row CT, but a statistically significant difference between the two techniques was not found by any of the three observers ($P > .05$). The nine false-negative lesions in seven patients at multi–detector row CT that were revealed at SPIO-enhanced MR imaging were hypovascular HCCs that measured less than 10 mm in diameter and had subtle low attenuation in at least one of four dynamic phases during retrospective review. All observers either regarded these lesions as cirrhosis-related benign nodules or missed these lesions at image interpretation. It is well known that detection and characterization of hypovascular HCC is sometimes difficult with dynamic CT or gadolinium-enhanced MR imaging (33–35). In our study, hypovascular lesions that were missed at multi–detector row CT were smaller than 1 cm in diameter and showed no capsular enhancement during the equilibrium phase. Therefore, when using only dynamic liver images, it is still difficult to accurately diagnose hypovascular liver lesions in patients with cirrhosis, even when high-temporal-resolution and high-spatial-resolution multi–detector row CT is used. In such cases, SPIO-enhanced MR imaging has some merits over multi–detector row CT.

Conversely, there were four lesions in four patients that were detected only at multi–detector row CT and not at SPIO-enhanced MR imaging. Those nodules were hypervascular HCCs that, when compared with the liver parenchyma at multi–detector row CT, showed hyperattenuation during the arterial phases and hypoattenuation or isoattenuation during the portal venous

Table 2

Sensitivity and Positive Predictive Value of SPIO-enhanced MR Imaging and Multi–Detector Row CT for the Detection of HCC

	Sensitivity per Lesion (%)*		Sensitivity per Patient (%)*		Positive Predictive Value†	
Observer	SPIO-enhanced MR Imaging	Multi–Detector Row CT	SPIO-enhanced MR Imaging	Multi–Detector Row CT	SPIO-enhanced MR Imaging	Multi–Detector Row CT
1	84.7 (50)	76.3 (45)	95.5 (42)	88.6 (39)	96.2 (2)	95.7 (2)
2	84.7 (50)	76.3 (45)	95.5 (42)	88.6 (39)	98.0 (1)	95.7 (2)
3	84.7 (50)	78.0 (46)	93.2 (41)	88.6 (39)	98.0 (1)	93.9 (3)

* Data in parentheses are the number of true-positive lesions.

† Data in parentheses are the number of false-positive lesions.

Figure 1

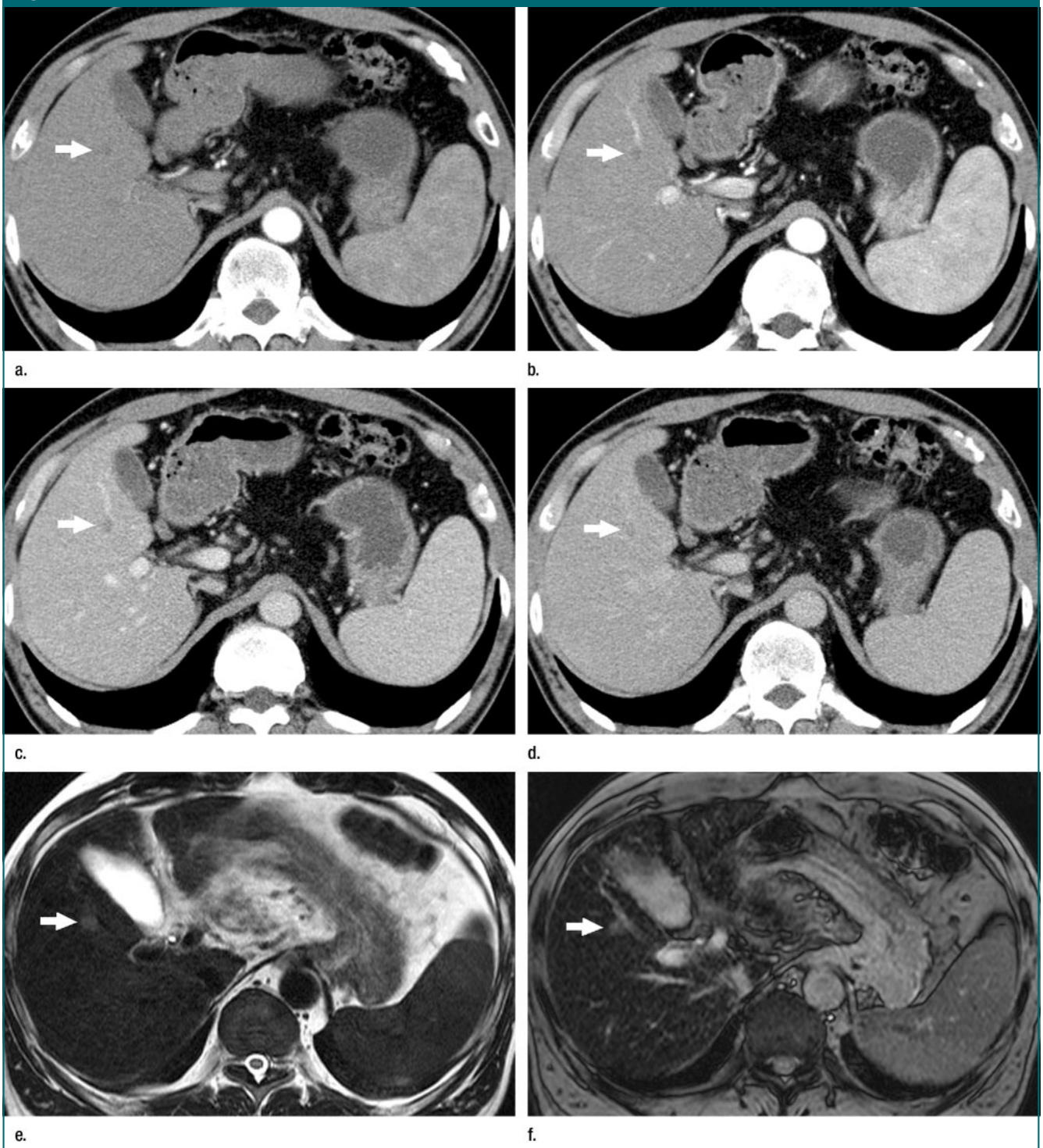

Figure 1: A 7-mm HCC nodule in 61-year-old man with chronic viral hepatitis. Transverse **(a)** early arterial, **(b)** late arterial, **(c)** portal venous, and **(d)** equilibrium phase CT scans show subtle low attenuation (arrow) in segment V, classified as a cirrhosis-related benign nodule by all observers. Transverse **(e)** SPIO-enhanced T2-weighted turbo spin-echo and **(f)** T2*-weighted FISP MR images show nodular hyperintensity (arrow) at same location as on **a–d**, classified as HCC by all observers.

Figure 2

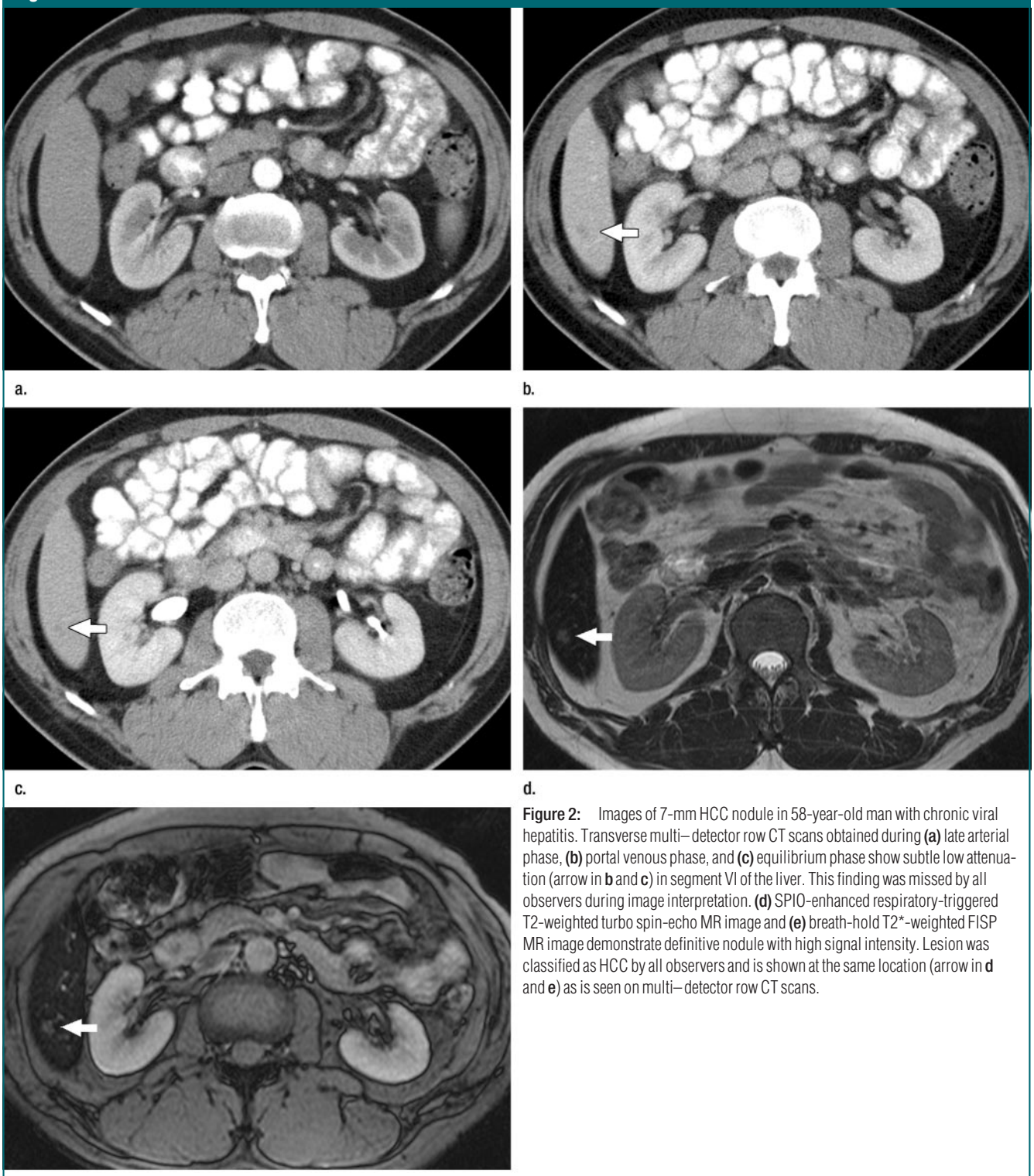

Figure 2: Images of 7-mm HCC nodule in 58-year-old man with chronic viral hepatitis. Transverse multi–detector row CT scans obtained during **(a)** late arterial phase, **(b)** portal venous phase, and **(c)** equilibrium phase show subtle low attenuation (arrow in **b** and **c**) in segment VI of the liver. This finding was missed by all observers during image interpretation. **(d)** SPIO-enhanced respiratory-triggered T2-weighted turbo spin-echo MR image and **(e)** breath-hold T2*-weighted FISP MR image demonstrate definitive nodule with high signal intensity. Lesion was classified as HCC by all observers and is shown at the same location (arrow in **d** and **e**) as is seen on multi–detector row CT scans.

Figure 3

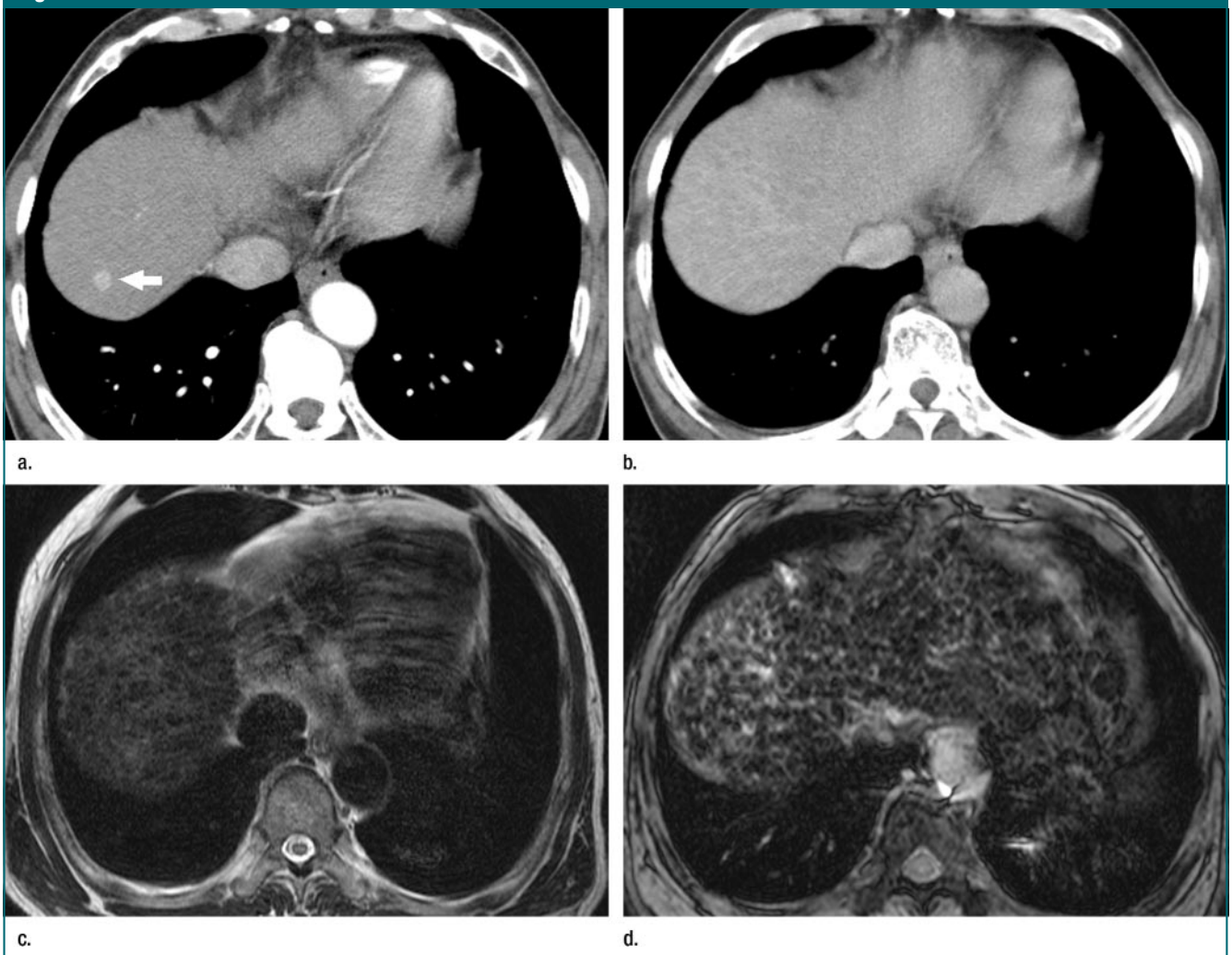

Figure 3: Images of HCC nodule in 55-year-old man with Child-Pugh class B cirrhosis. Transverse multi–detector row CT scans obtained during **(a)** late arterial phase and **(b)** equilibrium phase demonstrate hypervascular HCC (arrow) in the right lobe of the liver. Lesion could not be seen on **(c)** SPIO-enhanced respiratory-triggered T2-weighted turbo spin-echo MR image or **(d)** breath-hold T2*-weighted FISP MR image.

phase and equilibrium phase. When we retrospectively reviewed the four missed lesions at SPIO-enhanced MR imaging, all the lesions were masked by surrounding fibrosis or appeared as irregular and faint areas of high signal intensity with poor conspicuity. The major drawbacks of SPIO-enhanced MR imaging are the poor lesion conspicuity in late stage liver cirrhosis owing to fibrotic changes, the reduced uptake of iron oxide particles owing to the decreased activity of Kupffer cells compared with that of normal liver tissue, and the not infrequent uptake of iron oxide particles in well-differentiated HCC (36,37). The four patients with missed tumors at SPIO-enhanced MR imaging had Child-Pugh scores that were relatively higher (ie, scores of 8 or 9) than those of the majority of the other patients with Child-Pugh class A cirrhosis; this finding is well matched with the findings described in previous studies. Also, two of these patients with missed tumors had well-differentiated HCCs that might have contributed to the poor conspicuity of the lesion owing to a possible uptake of iron oxide particles by Kupffer cells in the HCC. Indeed, the majority of patients enrolled in our study had relatively well-preserved liver function that was classified as Child-Pugh class A cirrhosis, and this might be the one of main factors contributing to the better diagnostic performance of SPIO-enhanced MR imaging compared with multi–detector row CT.

Our study has limitations. First, not all lesions were surgically confirmed, which could potentially result in an overestimation of the actual sensitivity of both imaging modalities by reducing the number of false-negative lesions. Nevertheless, in our study, we included

Table 3

Level of Agreement between Observers with Regard to the Presence of HCC

Observer	SPIO-enhanced MR Imaging	Multi–Detector Row CT
1 vs 2	0.740	0.780
2 vs 3	0.792	0.725
1 vs 3	0.893	0.789

Note.—Data are κ values.

only those patients who had undergone surgery, who had not undergone surgery but who had undergone CT with iodized oil after transarterial chemoembolization or radiofrequency ablation with biopsy, or who had undergone follow-up multi–detector row CT or MR imaging at least 5 months after the initial imaging examination, during which the liver segment was ascertained to be free of clinically relevant lesions.

A second criticism of this study could be the relatively slow injection rate (3 mL/sec) of contrast material during dynamic CT. Given that we used a high concentration of iodine (ie, 370 mg iodine per milliliter), we could deliver a similar number of grams of iodine per second as other investigators who used a higher injection rate of 4 or 5 mL/sec.

Third, a selection bias for the initial referral for imaging may exist because most patients included in our study were suspected of having HCC on review of clinical and prior US findings. Therefore, lesions not apparent at US may be underrepresented in our study.

Fourth, a separate analysis for lesion detection comparing early and late arterial phases was not performed in this study. Although double arterial phase imaging could decrease the risk of inappropriate timing of arterial phase imaging, it may increase the radiation dose compared with single arterial phase imaging in patients with chronic liver disease who are at high risk for HCC; such patients should undergo periodic screening, including US or CT. Given that many hypervascular tumors are not markedly enhanced on early arterial phase images, the future development of optimized techniques for exact arterial phase imaging may decrease the clinical demand for double arterial phase imaging except for preoperative vascular mapping.

Last, in our study, 15 of 44 patients had two HCCs. Therefore, there might be a problem of data clustering in the alternative free-response ROC analysis, and there is a risk of overestimating the statistical significance (38,39). However, until now, there seems to be no perfect computer program to handle this problem of alternative free-response ROC analysis. To solve this problem, further improvements in programming will be necessary (40,41).

In summary, SPIO-enhanced MR imaging and multiphasic multi–detector row CT showed similar diagnostic accuracy and sensitivity for the detection of HCC in patients with mild liver cirrhosis on alternative free-response ROC analysis.

Acknowledgment: We thank Bonnie Hami, MA, for her editorial assistance and manuscript preparation.

References

1. Kobayashi K, Sugimoto T, Makino H, et al. Screening methods for early detection of hepatocellular carcinoma. Hepatology 1985; 5:1100–1105.
2. Choi BI. The current status of imaging diagnosis of hepatocellular carcinoma. Liver Transpl 2004;10(suppl 1):S20–S25.
3. Braga L, Guller U, Semelka RC. Modern hepatic imaging. Surg Clin North Am 2004;84: 375–400.
4. Okuda K, Ohtsuki T, Obata H, et al. Natural history of hepatocellular carcinoma and prognosis in relation to treatment: study of 850 patients. Cancer 1985;56:918–928.
5. Arii S, Okamoto E, Imamura M. Registries in Japan: current status of hepatocellular carcinoma in Japan—Liver Cancer Study Group of Japan. Semin Surg Oncol 1996;12:204–211.
6. Franco D, Usatoff V. Resection of hepatocellular carcinoma. Hepatogastroenterology 2001;48:33–36.
7. Colella G, Bottelli R, De Carlis L, et al. Hepatocellular carcinoma: comparison between liver transplantation, resective surgery, ethanol injection, and chemoembolization. Transpl Int 1998;11(suppl 1):S193–S196.
8. Poon RT, Fan ST, Tsang FH, Wong J. Locoregional therapies for hepatocellular carcinoma: a critical review from the surgeon's perspective. Ann Surg 2002;235:466–486.
9. Livraghi T, Goldberg SN, Lazzaroni S, Meloni F, Solbiati L, Gazelle GS. Small hepatocellular carcinoma: treatment with radiofrequency ablation versus ethanol injection. Radiology 1999;210:655–661.
10. Qin LX, Tang ZY. The prognostic significance of clinical and pathological features in hepatocellular carcinomas. World J Gastroenterol 2002;8:193–199.
11. Bellin MF, Zaim S, Auberton E, et al. Liver metastases: safety and efficacy of detection with superparamagnetic iron oxide MR imaging. Radiology 1994;193:657–663.
12. Soyer P. Will ferumoxides-enhanced MR imaging replace CT during arterial portography in the detection of hepatic metastases? prologue to a promising future. Radiology 1996; 200:610–611.
13. Choi D, Kim SH, Lim JH, et al. Preoperative detection of hepatocellular carcinoma: ferumoxides-enhanced MR imaging versus combined helical CT during arterial portography and CT hepatic arteriography. AJR Am J Roentgenol 2001;176:475–482.
14. Rofsky NM, Weinreb JC, Bernardino ME, Young SW, Lee JK, Noz ME. Hepatocellular tumors: characterization with Mn-DPDP-enhanced MR imaging. Radiology 1993;188: 53–59.
15. Spinazzi A, Lorusso V, Pirovano G, Kirchin M. Safety, tolerance, biodistribution and MR imaging enhancement of the liver with gadobenate dimeglumine: results of clinical pharmacologic and pilot imaging studies in nonpatient and patient volunteers. Acad Radiol 1999;6:282–291.
16. Vogl TJ, Pegios W, McMahon C, et al. Gadobenate dimeglumine: a new contrast agent for MR imaging—preliminary evaluation in healthy volunteers. AJR Am J Roentgenol 1992;158:887–892.
17. Hu H, He HD, Foley WD, Fox SH. Four multidetector-row helical CT: image quality and volume coverage speed. Radiology 2000; 215:55–62.
18. Berland LL, Smith JK. Multidetector-array CT: once again, technology creates new opportunities. Radiology 1998;209:327–329.
19. Murakami T, Kim T, Takamura M, et al. Hypervascular hepatocellular carcinoma: detection with double arterial phase multidetector row helical CT. Radiology 2001; 218:763–767.
20. Lee JM, Kim IH, Kwak HS, Youk JH, Han

YM, Kim CS. Detection of small hypervascular hepatocellular carcinoma in cirrhotic patients: comparison of superparamagnetic iron oxide-enhanced MR imaging with dual-phase spiral CT. Korean J Radiol 2003;4:1–8.

21. Hori M, Murakami T, Kim T, et al. Detection of hypervascular hepatocellular carcinoma: comparison of SPIO-enhanced MRI with dynamic helical CT. J Comput Assist Tomogr 2002;26:701–710.

22. Reimer P, Jahnke N, Fiebich M, et al. Hepatic lesion detection and characterization: value of nonenhanced MR imaging, superparamagnetic iron oxide-enhanced MR imaging, and spiral CT-ROC analysis. Radiology 2000;217:152–158.

23. Kang BK, Lim JH, Kim SH, et al. Preoperative depiction of hepatocellular carcinoma: ferumoxides-enhanced MR imaging versus triple-phase helical CT. Radiology 2003;226:79–85.

24. Pugh RN, Murray-Lyon IM, Dawson JL, Pietroni MC, Williams R. Transection of the esophagus for bleeding esophageal varices. Br J Surg 1973;60:646–649.

25. Lencioni R, Pinto F, Armillotta N, et al. Intrahepatic metastatic nodules of hepatocellular carcinoma detected at lipiodol-CT: imaging-pathologic correlation. Abdom Imaging 1997;22:253–258.

26. Chakraborty DP, Winter LH. Free-response methodology: alternate analysis and a new observer-performance experiment. Radiology 1990;174:873–881.

27. Metz CE. ROC methodology in radiologic imaging. Invest Radiol 1986;21:720–733.

28. Dwyer AJ. Matchmaking and McNemar in the comparison of diagnostic modalities. Radiology 1991;178:328–330.

29. Landis JR, Koch GG. The measurement of observer agreement for categorical data. Biometrics 1977;33:159–174.

30. Furuta A, Ito K, Fujita T, Koike S, Shimizu A, Matsunaga N. Hepatic enhancement in multiphasic contrast-enhanced MDCT: comparison of high- and low-iodine-concentration contrast medium in same patients with chronic liver disease. AJR Am J Roentgenol 2004;183:157–162.

31. Fretz CJ, Elizondo G, Weissleder R, Hahn PF, Stark DD, Ferrucci JT Jr. Superparamagnetic iron oxide-enhanced MR imaging: pulse sequence optimization for detection of liver cancer. Radiology 1989;172:393–397.

32. Kim SH, Choi DI, Lim JH, et al. Optimal pulse sequence for ferumoxides-enhanced MR imaging used in the detection of hepatocellular carcinoma: a comparative study using seven pulse sequences. Korean J Radiol 2002;3:87–97.

33. Honda H, Kaneko K, Maeda T, et al. Small hepatocellular carcinomas undetected on two-phased incremental computed tomography: angiographic and clinicopathologic findings. Invest Radiol 1995;30:458–465.

34. Matsui O, Kadoya M, Kameyama T, et al. Benign and malignant nodules in cirrhotic livers: distinction based on blood supply. Radiology 1991;178:493–497.

35. Hayashi M, Matsui O, Ueda K, Kawamori Y, Gabata T, Kadoya M. Progression to hypervascular hepatocellular carcinoma: correlation with intranodular blood supply evaluated with CT during intraarterial injection of contrast material. Radiology 2002;225:143–149.

36. Elizondo G, Weissleder T, Stark DD, et al. Hepatic cirrhosis and hepatitis: MR imaging enhanced with superparamagnetic iron oxide. Radiology 1990;174:797–801.

37. Imai Y, Murakami T, Yoshida S, et al. Superparamagnetic iron oxide-enhanced magnetic resonance images of hepatocellular carcinoma: correlation with histologic grading. Hepatology 2000;32:205–212.

38. Obuchowski NA. Receiver operating characteristic curves and their use in radiology. Radiology 2003;229:3–8.

39. Zweig MH, Campbell G. Receiver-operating characteristic (ROC) plots: a fundamental evaluation tool in clinical medicine. Clin Chem 1993;39:561–577.

40. Stephan C, Wesseling S, Schink T, Jung K. Comparison of eight computer programs for receiver-operating characteristic analysis. Clin Chem 2003;49:433–439.

41. Chakraborty DP, Berbaum KS. Observer studies involving detection and localization: modeling, analysis, and validation. Med Phys 2004;31:2313–2330.